Co-seismic strike–slip fault displacement determined from push-up structures: the Selsund Fault case, South Iceland

Jacques Angelier[a,b,*], Françoise Bergerat[a], Magalie Bellou[a,b], Catherine Homberg[a]

[a]*Laboratoire de Tectonique, Université Pierre-et-Marie Curie, UMR 7072, Boîte 129, 4, place Jussieu, 75252 Paris cedex 05, France*
[b]*Observatoire Océanologique de Villefranche, UFR 939 Université Pierre-et-Marie Curie and UMR 6256 Géosciences Azur, BP 127, 06230 Villefranche-sur-Mer, France*

Abstract

We analysed push-up structures along the Selsund Fault, a N–S right-lateral strike-slip fault activated during the 1912 earthquake in the South Iceland Seismic Zone. Volume changes and syn-tectonic collapse affected push-ups during the earthquake, followed by post-seismic gravitational sagging. To determine the push-up shortening, and hence the strike–slip fault motion, we define a virtual push-up structure, without volume change and collapse, and we compare it with the present-day configuration. Whereas length comparisons are subject to errors, volumetric analysis allows determination of shortening through evaluation of the thickness of the deformed layer affected by the push-ups. We determine a co-seismic peak displacement of 2.4 m along the rupture trace. This value is consistent with the magnitude 7 of the earthquake, based on empirical relationships. Neglecting volume changes and collapse effects gives underestimated displacement. The new method for analysing push-up structures thus allows better determination of magnitudes of ancient earthquakes along strike–slip faults.
© 2003 Elsevier Ltd. All rights reserved.

Keywords: Earthquake; Rupture trace; Seismotectonics; Strike–slip; Push-up structure; Magnitude; Iceland

1. Introduction

Along earthquake rupture traces of reverse or normal faults, vertical offsets allow determination of the fault motion in three dimensions, provided that the attitude of the slip vector is known. In contrast, the vertical components along strike–slip rupture traces are often small and variable, with reversals over short distances. Direct determination of the strike–slip motion is possible where man-made features or steeply dipping geological structures are cut by the fault. This was the case in asphalted car park areas cut by the oblique reverse fault of the 21 September 1999 earthquake in Taiwan (Angelier et al., 2003a) and a left-lateral strike–slip fault of the 21 June 2000 earthquake in South Iceland (Angelier and Bergerat, 2002).

Difficulties in the determination of strike–slip offsets along earthquake rupture traces arise where such markers are absent. It is, however, essential to determine displacement along seismic strike–slip faults, which constrains empirical relationships between fault offset and earthquake magnitude. Evaluating the size of the largest earthquakes that occurred in an active fault zone is a major target in earthquake hazard studies. Using instrumentally recorded earthquakes only may result in severe underestimation of the largest expectable magnitudes.

We aim at determining the strike–slip displacement along earthquake rupture traces, based on structural analysis applied to push-up structures (Fig. 1). We will show that without special considerations on push-up geometry and evolution the analysis may be biased and the displacement underestimated. We focus on the right-lateral Selsund Fault zone (Einarsson and Björnsson, 1979; Bjarnason et al., 1993), activated during the largest instrumentally recorded earthquake in South Iceland, the 1912 earthquake of approximate magnitude 7 (Karnik, 1969). The first aim of this paper is to demonstrate that the analysis of the push-up structures allows accurate reconstruction of the fault offset,

* Corresponding author. Correspondence address: Laboratoire de Tectonique, Université Pierre-et-Marie Curie, UMR 7072, Boîte 129, 4, place Jussieu, 75252 Paris cedex 05, France. Fax: +33-1-44275085.

E-mail address: jacques.angelier@lgs.jussieu.fr (J. Angelier).

Nomenclature

D	displacement on earthquake strike–slip fault (m)
D_{max}	peak displacement of earthquake (m)
d	lateral offset of en-échelon surface faults (m)
ϕ	angle between en-échelon segments and strike–slip fault (°)
θ	angle between push-up–perpendicular trend and strike–slip fault trend (°)
η	angle between oblique and strike–perpendicular push-up cross-sections (°)
W	present-day width of push-up structure, W_{obl} in oblique section (m)
W_0	width of push-up structure before deformation, W_{0obl} in oblique section (m)
H_{max} and H_{min}	height of push-up hillock on highest and lowest sides, respectively (m)
L	cross-sectional length of push-up top surface (m)
L'	cross-sectional length of push-up top surface just after earthquake (m)
S	present-day volume of push-up hillock per unit length, S_{obl} in oblique section (m²)
S_{max}	present-day volume of push-up hillock per unit length, relative to lowest side (m²)
S^*	virtual volume of push-up hillock per unit length, without volume change (m²)
S'	volume of push-up hillock per unit length, just after earthquake (m²)
S_T	final volume of deformed rock per unit length of push-up (m²)
S_T^*	final volume of intact rock per unit length of push-up (m²)
T	thickness of layer affected by push-ups (m)
T_{max}	largest acceptable thickness of layer affected by push-ups (m)
ΔW	across-strike horizontal shortening of push-up, in absolute value (m)
λ_a	average ratio between present-day and pre-earthquake densities, whole push-up structure
λ_s	near-surface present-day density ratio in most deformed domains near push-up top
λ	density ratio at each point of push-up structure
k	reference number of profile segment, from one to K
w_k	horizontal width of profile segment (m)
q_k	height of profile segment above oblique push-up base (m)
q_{max}	height of profile segment above oblique push-up base below push-up top (m)
a and b	coefficients of linear relationship between D and T^{-1} (a in m², b in m)
Δa and Δb	standard deviations of a and b (Δa in m², Δb in m)
r_i	radius of element i in push-up model section (m)
w_i	horizontal width of element i in push-up model section (m)
h_i	height of element i in push-up model section (m)
α and β	fold angles of elements in push-up model section (°)
E	difference in height between push-up sides in push-up model section (m)
F_a and F_b	dimensionless functions that depend on folding sub-mode
ω	dummy angle used in functions F_a and F_b (radians)
C	(C_a and C_b depending on folding sub-mode) peak collapse in push-up model (m)
M	moment magnitude of earthquake

provided that specific phenomena like co-seismic dilation and post-seismic collapse are taken into account. The results will be used to check empirical relationships between the offset and the magnitude, which in this case is known.

2. The South Iceland Seismic Zone

In Iceland, located on the Mid-Atlantic Ridge, plate separation occurs at a rate of 18 mm/yr along the N105°E direction (DeMets et al., 1990, 1994). Both the spreading of the Mid-Atlantic Ridge and the location above the Iceland Mantle Plume control the tectonic and magmatic activity in Iceland (Fig. 2a). Because the Mid-Atlantic Ridge is moving

westwards with respect to the plume, a new rift zone developed above the apex of the plume when the plate boundary migrated to a critical distance to the west. Thus, the rift system in Iceland has repeatedly been shifted eastwards during the Late Cenozoic, whereas the location of oceanic accretion remained stable along the Kolbeinsey and Reykjanes oceanic ridges, north and south off Iceland. As a consequence, two major ocean-ridge transform zones developed: the Tjörnes Fracture Zone to the north and the left-lateral South Iceland Seismic Zone (Fig. 2a).

At the western tip of the South Iceland Seismic Zone (SISZ), the Reykjanes Peninsula is the on-land extension of the Reykjanes Ridge (Fig. 2b). At the eastern tip of the SISZ, the Eastern Volcanic Zone became active 2–3 million
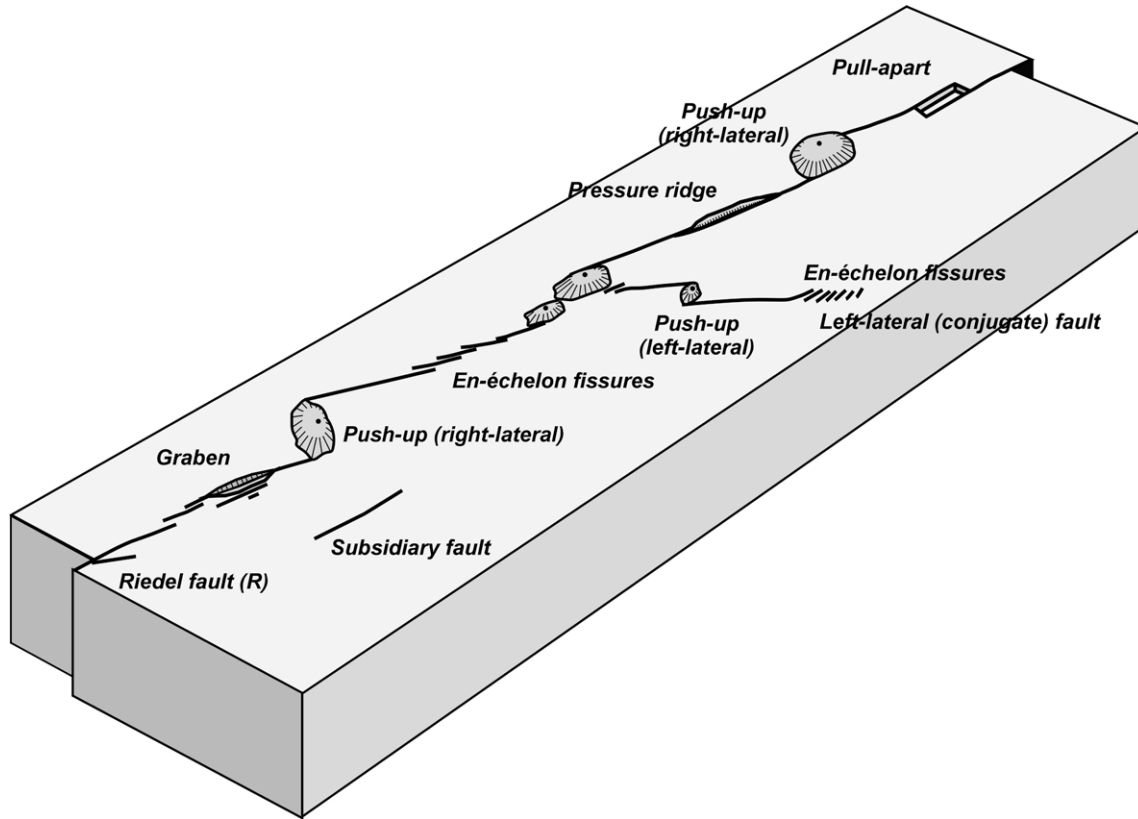
Fig. 1. Common features along a right-lateral rupture trace of earthquake in Iceland.
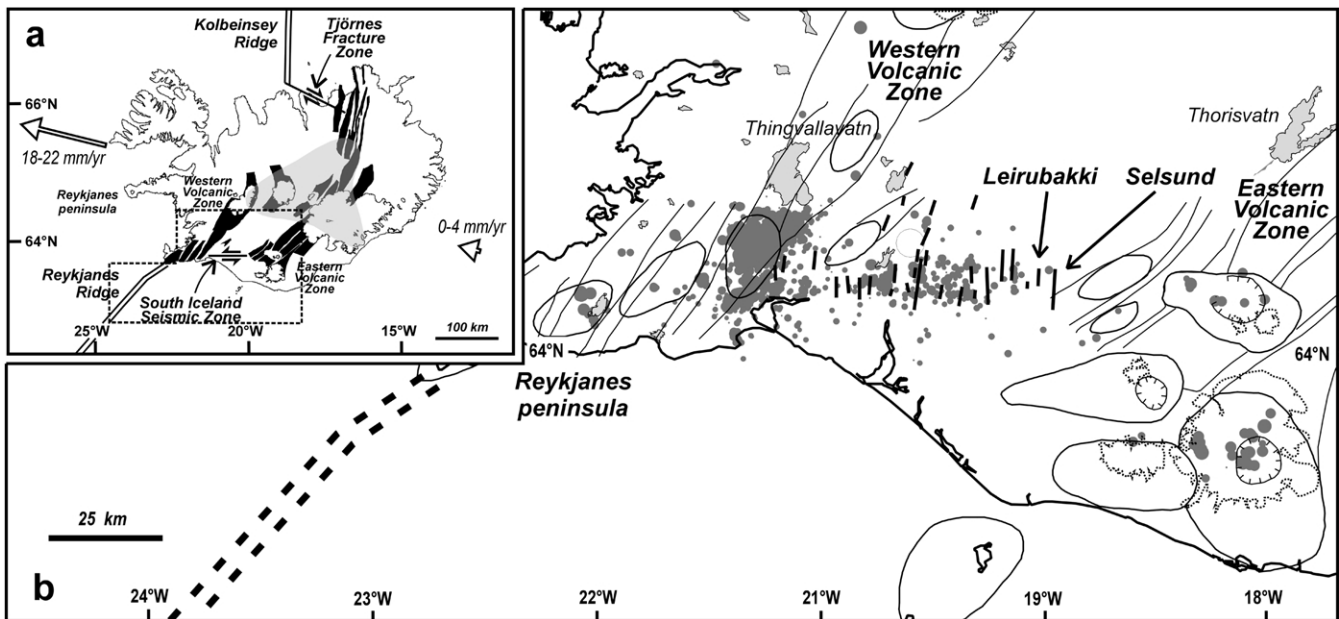

Fig. 2. Geological setting of the studied area. (a) Plate boundaries in Iceland. In black: main Holocene volcanic systems of onshore rift zones (after Saemundsson, 1979). Double lines offshore: ocean ridge axes. Open arrows: plate velocities (relative to Iceland Mantle Plume), accounting for a divergence rate of 18 mm/yr (DeMets et al., 1990, 1994). Light grey: postulated hot spot extension at 400 km depth (after Tryggvason et al., 1983). Location of map (b) as dashed frame. (b) The South Iceland Seismic Zone. Approximate location of Kolbeinsey ridge: thick dashed lines. Boundaries of fissure swarms in rift segments as thin lines. Thin elliptical lines bound major Holocene volcanic systems (after Saemundsson, 1979). Main active faults of the South Iceland Seismic Zone as thick lines (after Einarsson, 1991). Grey dots: earthquakes with magnitudes larger than 0.5 during the year 1995 (after Bergerat et al., 1998; from SIL network database of Stefansson et al. (1993)). Lakes in light grey, thin dotted lines around glaciers.
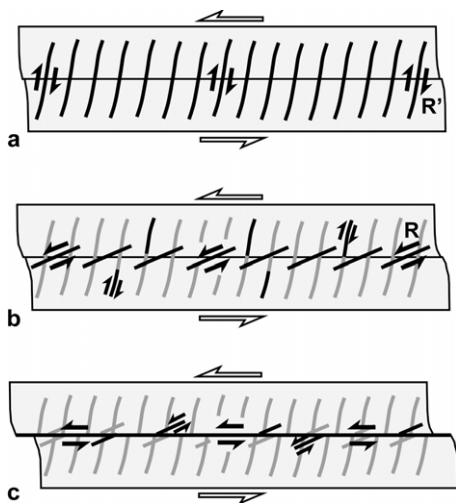
Fig. 3. Development of a major left-lateral strike–slip shear zone like the South Iceland Seismic Zone. (a) First stage, most faults as densely spaced N10°E dextral R′-type faults. (b) Second stage with N70°E sinistral R-type faults. (c) Mature stage, major E–W fault expressed.

years ago (Jóhannesson et al., 1990). The development of the SISZ (Gudmundsson and Brynjolfsson, 1993) results from this rift jump. The seismological network in South Iceland (Stefansson et al., 1993) reveals that the seismicity of the SISZ concentrates in an E–W-trending zone about 20 km wide and 70 km long (Fig. 2b). However, the distribution of faults and damage zones of historical earthquakes suggests a width larger than 20 km (Gudmundsson, 1995). During the last few centuries, sequences of large earthquakes ($M = 6–7$) occurred in the SISZ at intervals of 45–112 years (Björnsson, 1975; Einarsson and Björnsson, 1979; Stefansson, 1979; Einarsson et al., 1981).

A surprising feature of the SISZ is the distribution of the active strike–slip deformation, which involves few left-lateral faults but many N–S-trending right-lateral ones (Einarsson et al., 1981; Einarsson and Eiriksson, 1982b). This fault pattern is related to the immature character of the SISZ as a left-lateral transform zone (Bergerat and Angelier, 1999, 2000). We interpret it in terms of the development of a left-lateral strike–slip fault zone as follows.

First, narrow-spaced right-lateral faults (R′ type) appear, and trend oblique at high angles with respect to the main shear zone (Fig. 3a). The present-day SISZ well illustrates this first stage, with numerous N10°E striking right-lateral faults. Second, left-lateral faults (R type) develop, and trend oblique at small angles as compared with the main shear zone (Fig. 3b). The presence of N70°E left-lateral faults (Bergerat et al., 1998) indicates that the SISZ has reached this second stage. Third, as deformation continues, new left-lateral strike–slip faults develop, similar in direction to the main shear zone (Fig. 3c). Major E–W left-lateral faults, which would characterise this mature stage, are almost absent in South Iceland, showing that the SISZ has not reached this third stage. The shear zone development

described above (Fig. 3) is compatible with a Riedel's type distribution of faults, the results of analogue modelling and studies along other seismic faults (Riedel, 1929; Tchalenko and Ambraseys, 1970).

3. The Selsund Fault

We study the 1912 rupture trace of the Selsund Fault (Einarsson et al., 1981; Einarsson and Eiriksson, 1982a,b; Bjarnason et al., 1993; Bellou, 2002). The rupture traces affect soils, Pahoehoe-type lavas and tuffs over a N–S distance of about 10 km (Fig. 4). We analyse three major segments where push-ups of the 1912 earthquake occur, as shown by Bjarnason et al. (1993). These major segments make an average clockwise angle of 15° with the inferred N–S trend of the Selsund Fault (Fig. 4a). Each major segment is composed of en-échelon surface faults that trend N20–30°E, with fractures and fissures that are in turn distributed en-échelon. Near the surface, push-ups are observed between small en-échelon segments, as isolated hillocks above the flat surface of the lava flows or tuff layers (Fig. 5).

Push-ups are common along active faults of Iceland (Einarsson and Eiriksson, 1982b; Bjarnason et al., 1993; Bergerat et al., 2003). They connect individual segments of en-échelon faults, and result from compression between the blocks (Fig. 6). As a result, their shortening depends on the strike–slip displacement. The push-up structure affects the near-surface level in which en-échelon fissures develop, and should not be extrapolated below this level. To be consistent, the geometrical analysis of strike–slip displacement should not mix observations at different depths. To be reliable, the results should not depend on uncontrolled assumptions about the deep structure. Our analysis is made near the surface, along the earthquake rupture trace (Fig. 6a). No data are available concerning the structure at depth. Because the earthquake fault is pure strike–slip in type, the study can be performed in terms of horizontal plane deformation. The non-deformed blocks on both sides of the fault are considered rigid.

In Iceland, push-ups affect the soil and, in many cases, the uppermost basalt flow, or group of basalt flows. Along the Selsund Fault, the shallow level deformation is illustrated by the limited width of the push-ups, 4–40 m, incompatible with deep roots (Fig. 6a). Whether the change from en-échelon segments to deeper faults occurs abruptly (Fig. 6) or progressively (via a twist angle) is unknown and has little importance for our reconstruction. Mechanically weak soil or tuff levels between basalt flows facilitate the inferred décollement. In this paper, the thickness of the layer affected by the push-ups is T and the offset of the underlying strike–slip fault is D (Fig. 6a). All symbols used throughout this paper are listed in the Nomenclature.
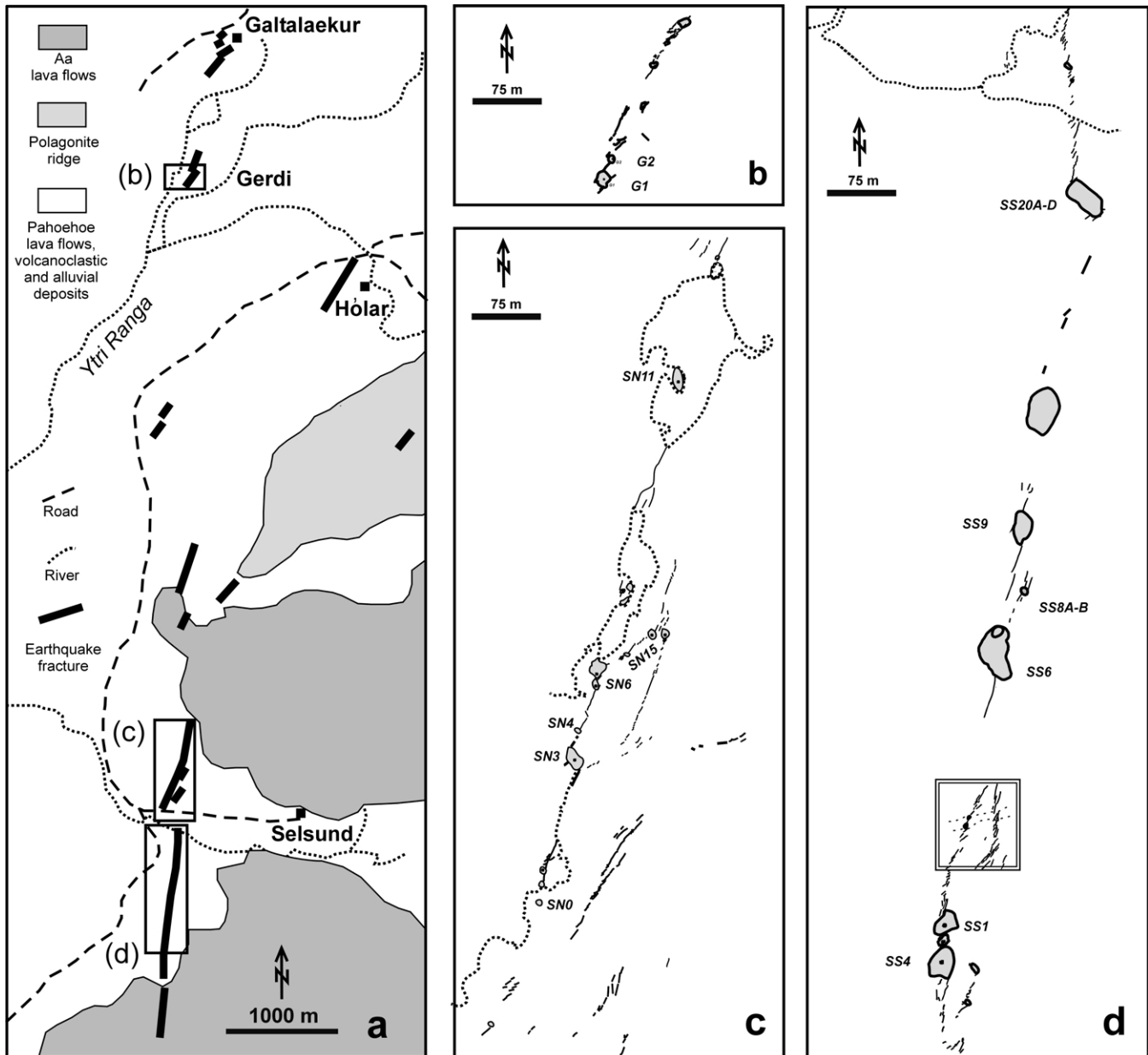
Fig. 4. Map of earthquake fault traces with push-up structures, produced by the 1912 earthquake near Selsund. (a) General map of the Selsund Fault, modified after Bjarnason et al. (1993). Location of detailed maps as thin rectangular frames. (b)–(d) Detailed maps of the three segments considered in this study, Gerdi, N-Selsund and S-Selsund, respectively (Bellou, 2002). Thin double frame in (d): location of Fig. 14. Push-up names as in Fig. 8.

4. Strike–slip displacement inferred from push-up shortening

Although the push-ups result from strike–slip related compression, their across-strike shortening, ΔW, is not the strike–slip fault displacement, D. Most push-up structures strike oblique to the trend of the deep strike–slip fault. With respect to the trend of the underlying strike–slip fault, two angles in the horizontal plane are involved (Fig. 6). The first angle, ϕ, describes the obliquity of en-échelon segments. The second angle, θ, describes the obliquity of the direction perpendicular to push-up strike. Common situations involve an angle θ larger (Fig. 6c), or in rare cases smaller, than ϕ.

Large angles θ do not deserve consideration because elongated compressive structures making small angles with the fault are pressure ridges, not push-ups. We adopt a simplified relationship between D and ΔW:

$$\Delta W = D\cos\theta \tag{1}$$

We reconstruct the push-up structure in vertical cross-sections (Fig. 7). The main data are the push-up width, W, the cross-sectional length of the push-up top surface, L, and the present-day volume of the push-up hillock per unit length, or 'excess section', S (Fig. 7c). Note that all terms of S-type are volumes divided by unit length of push-up, in a section perpendicular to push-up axis, and will be named
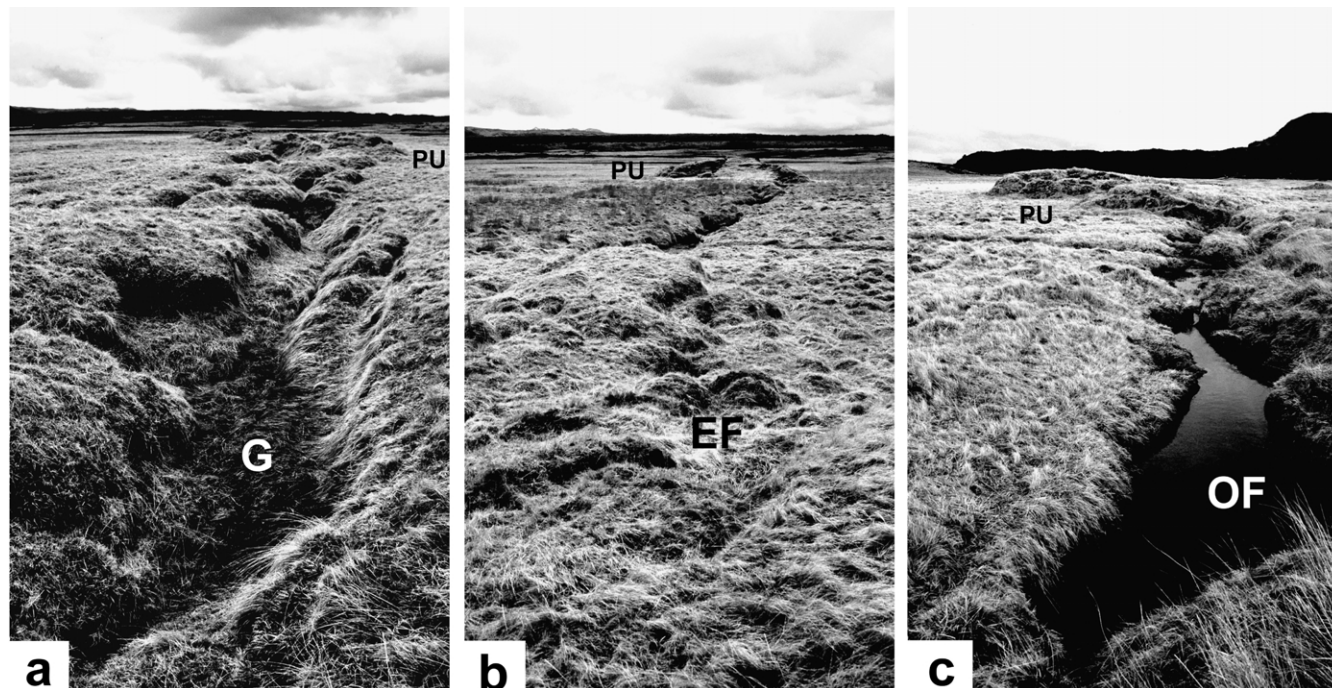
Fig. 5. Photographs (taken in 2002) of earthquake fault traces with push-ups, produced by the 1912 earthquake near Selsund. G—fault-parallel graben, EF—en échelon fissures, OF—open fracture, PU—push-up. Push-ups are left stepping, indicating right-lateral motion.

'volumes' (although they are given in m²). This simplification results from the plane strain assumption in vertical axis-perpendicular push-up sections. The absolute value of the shortening across the push-up, ΔW, is given by:

$$\Delta W = W_0 - W \qquad (2)$$

where W is the present-day width of the push-up structure

(Fig. 7c) while W_0 is the corresponding width before deformation (Fig. 7a).

Had no significant volume change occurred during and after deformation, the volume per unit length of push-up hillock would not be S (actually measured), but S^* (Fig. 7b):
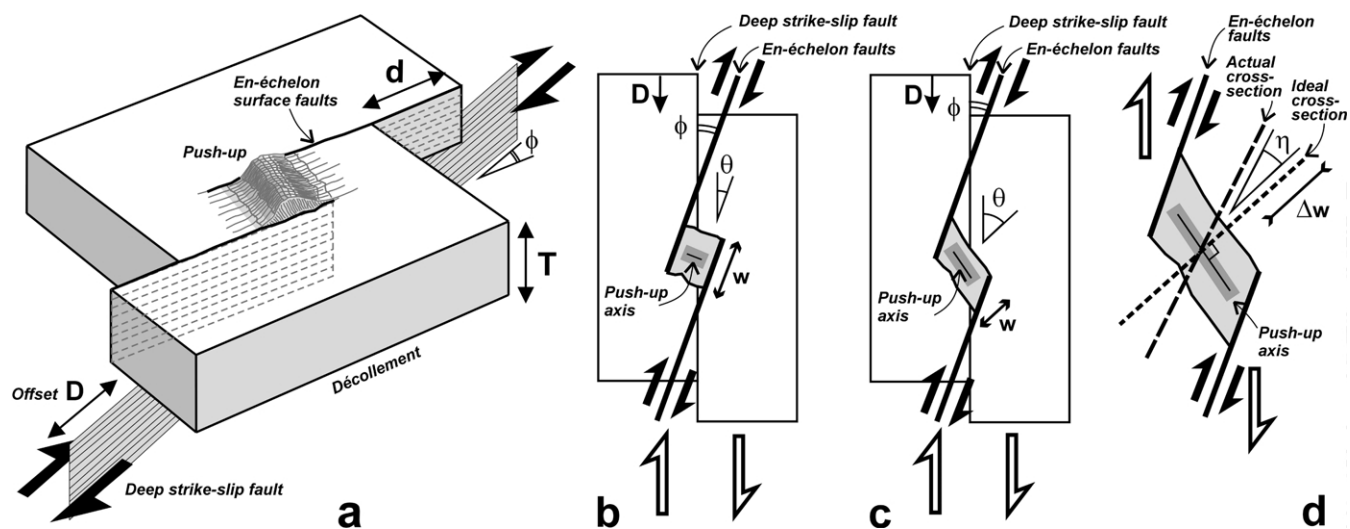
$$S^* = T\Delta W \qquad (3)$$

Fig. 6. Geometry of surface faults, push-up and underlying strike–slip fault. (a) Schematic push-up structure (modified after Bergerat et al., 2003): *D*, offset of strike–slip fault; *d*, lateral offset of en-échelon surface faults (dilation not shown); *T*, thickness of layer forming the push-up; *φ*, obliquity of en-échelon segments with respect to the parent fault. (b) and (c) map views, with push-up in grey: *W*, push-up width; *ΔW*, shortening across push-up; *θ*, angle between direction perpendicular to push-up axis and trend of strike–slip fault; *D* and *φ* as in (a). (d) Obliquity of cross-sections: *η*, angle between real and ideal sections; W_{obl} and *W*, apparent and actual push-up widths. (b)–(d) Illustrate horizontal plane deformation in the uppermost level, regardless of the structural changes with depth, abrupt (a) or not.
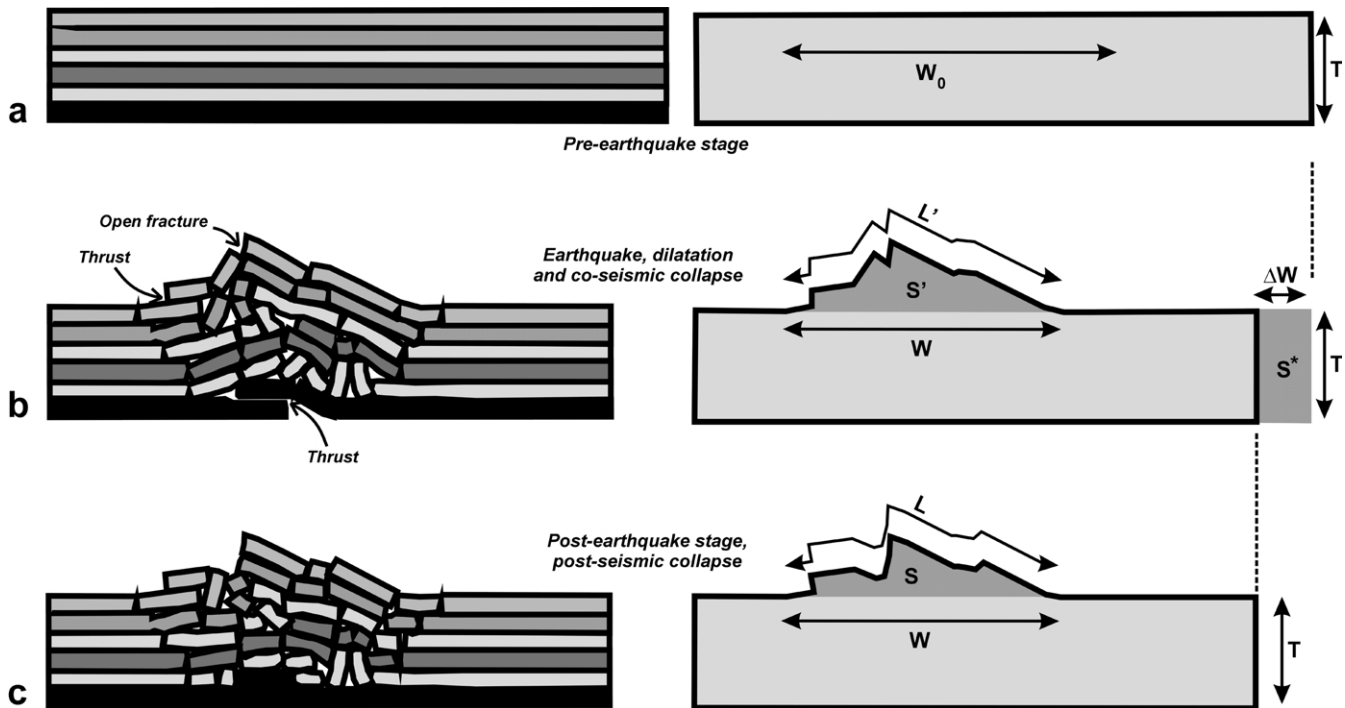
Fig. 7. Principle of the determination of shortening and depth to décollement across a push-up structure (modified after Bergerat et al., 2003). Cross-sections perpendicular to push-up axis. On left, sections showing (a) pre-earthquake section in lava flows, (b) push-up just after the earthquake, with disruption of basalt plates and initial collapse, and (c), present-day push-up configuration after post-earthquake collapse. On right, schematic sections for the same steps, with T as the layer thickness, showing in (a) pre-earthquake width, W_0, of the future push-up domain, in (b) push-up width W, hillock section S', profile surface length L' and shortening ΔW, and in (c) final hillock section S and profile surface length L. Same symbols as in text.

For the small push-ups affecting grassy soils during the June 2000 earthquakes in South Iceland (Bergerat and Angelier, 2001, 2003), the volume changes were negligible. This is generally not the case for older and larger push-ups. Their present-day volume per unit length, S, substantially differs from the pre-earthquake volume, S^*. Even the value just after the earthquake, S' in Fig. 7b, differs from both S and S^*, because of co-seismic dilatation and initial (co-seismic) collapse. Co-seismic expansion of deformed rock mass is revealed by open gaps between broken basalt slabs in push-ups. Initial collapse during the earthquake was a result of fracturing that produced these slabs. In addition, post-seismic gravitational sagging of push-ups has been reported in South Iceland (Bjarnason et al., 1993).

Considering the push-up sections before and after the earthquake (Fig. 7), and assuming that $L = W_0$, the difference between L and W is the shortening according to Eq. (2). This is an approximation because of the volume changes discussed above and other factors discussed later (Section 6). The present-day surface length of push-up section, L, the length just after the earthquake, L', and the corresponding pre-earthquake width, W_0, may differ (Fig. 7, compare parts a–c). Any use of Eqs. (3) or (4) to quantify the push-up shortening, and hence the strike–slip displacement, thus requires evaluation of the pre-earthquake width, W_0, or the pre-earthquake rock volume per unit length, S^*. Other values, L and S, respectively, are measured (Fig. 7). As the determination of W_0 as a function of L is subject to

errors, the relation between S^* and S, which depends on T, is crucial.

Fig. 7 shows an 'ideal' cross-section, perpendicular to push-up axis. In the field, all cross-sections could not be traced exactly perpendicular to push-up axes. The reconstruction of the ideal cross-section implied minor preliminary correction of the data:

$$W = W_{obl}\cos\eta, \quad W_0 = W_{0obl}\cos\eta, \quad S = S_{obl}\cos\eta \qquad (4)$$

where η is the angle between actual and ideal cross-sections (Fig. 6d). W_{obl}, W_{0obl} and S_{obl} were measured in the oblique section, whereas W, W_0 and S refer to the ideal section.

5. The Selsund data

A general map of the fault trace was given by Bjarnason et al. (1993). We mapped in detail three main segments (Fig. 4), with a GPS differential system (Bellou, 2002). The 18 push-up profiles of Fig. 8 and Table 1 were acquired with a rigid rule and a dipmeter, as successions of 9–37 straight segments (23 on average) with measured length and plunge. Their lengths range between 8 and 40 m (22 m on average). The maximum push-up height, 1.8 m on average, ranges between 0.4 and 3 m. The uncertainties on the measured values of W, L and S (Table 1 and Fig. 7c) are smaller than 0.2 m for lengths and 1 m² for volumes per unit length.

One may tentatively evaluate the push-up shortening,

Table 1

Main parameters measured in push-up profiles of Fig. 8. Ref.—reference number of push-up profile; prefixes G, SN and SS refer to fault segments near Gerdi, N-Selsund and S-Selsund, respectively (Fig. 4). K, number of measured segments in each profile; θ, angle between the strike–slip fault at depth (trending N26°E for Gerdi, N16°E for N-Selsund and N8°E for S-Selsund) and the direction perpendicular to each push-up axis (as defined in Fig. 6); W, profile length; L, cross-sectional length of push-up top surface (Fig. 7); S_{max} and S, along-profile volume per unit length (S_{max} with horizontal base at lowest profile tip level and S with oblique base connecting profile tips); H_{max} and H_{min}, push-up heights measured on highest and lowest sides, respectively; ΔW, shortening estimated according to Eq. (2) under the assumption $L = W_0$; D, estimated offset of strike–slip fault, calculated as a function of ΔW and θ based on Eq. (1); T, estimated depth to décollement evaluated according to Eq. (3), under the constant volume assumption. These values are generally underestimated for ΔW and D, and overestimated for T, as discussed in the text

Ref.	K	θ (°)	W (m)	L (m)	S_{max} (m²)	S (m²)	H_{max} (m)	H_{min} (m)	ΔW (m)	D (m)	T (m)
G2	15	0	12.43	13.32	9.95	7.78	1.69	1.35	0.89	0.89	9
G1	20	4	21.14	21.65	18.72	15.56	1.97	1.68	0.51	0.51	31
SN15	21	25	20.08	20.62	13.17	11.02	1.78	1.56	0.54	0.60	20
SN11	24	32	23.01	24.42	37.22	35.18	3.07	2.89	1.41	1.67	25
SN6	28	24	26.67	27.35	33.09	30.98	2.06	1.90	0.69	0.75	45
SN4	13	2	12.25	12.88	10.75	7.50	1.47	0.94	0.62	0.62	12
SN3	21	4	19.59	20.90	25.75	22.50	2.44	2.11	1.31	1.31	17
SN0	21	1	14.03	14.76	10.78	8.69	1.72	1.42	0.73	0.73	12
SS20A	27	18	29.14	29.70	30.64	25.78	2.04	1.71	0.56	0.59	46
SS20B	26	11	23.45	24.04	27.43	24.51	2.01	1.76	0.59	0.60	42
SS20C	25	10	25.73	26.17	28.69	22.94	1.95	1.50	0.44	0.45	52
SS20D	26	4	26.04	26.42	22.89	20.34	1.75	1.56	0.38	0.38	53.
SS9	25	29	28.13	28.39	23.55	22.75	1.58	1.52	0.26	0.30	86
SS8A	9	6	8.39	8.52	3.07	1.92	0.45	0.72	0.13	0.13	14
SS8B	12	21	8.39	8.65	5.44	2.91	1.06	0.46	0.25	0.27	12
SS6	36	28	38.00	38.66	47.61	45.71	2.62	2.52	0.66	0.75	69
SS1	32	27	33.10	33.37	41.36	29.99	1.95	1.27	0.27	0.30	112
SS4	37	39	39.92	40.06	29.82	27.51	1.31	1.19	0.14	0.18	192

ΔW, by comparing W and L (Table 1). Assuming plane strain in section and conservation of length and volume (so that $L = W_0$ and $S = S^*$), the results of Table 1 were obtained as follows. First, the shortening, ΔW, was determined from Eq. (2). Second, the displacement of the strike–slip fault, D, was given by Eq. (1). Third, the thickness of the deformed layer, T, was given by Eq. (3).

Most push-ups are located along the main right-lateral fault (Fig. 4). Push-up SN15 is located on a left-lateral fault. Push-up SS8A-B is located on a subsidiary right-lateral fault. Multiple faults and fissures have accommodated a significant part of the displacement around push-ups SN4 and SS4. The displacement values obtained from the 10 remaining push-ups show large dispersion (0.18–1.67 m). Four profiles across push-up SS20 yielded more homogeneous values (0.30–0.60 m), showing that other causes than data uncertainty control this dispersion.

The strike–slip displacement thus estimated (Table 1) averages 0.71 m (0.70, 1.02 and 0.41 m for the Gerdi, N-Selsund and S-Selsund segments, respectively). These values are surprisingly low considering the 3-m-displacement evaluated by Bjarnason et al. (1993), based on a sheep track offset along the S-Selsund rupture trace. Along the N-Selsund rupture trace, the average displacement (1.02 m) that we determined is close to the value of 1.25 m calculated by Bjarnason et al. (1993) from observations on the two largest push-ups. The thickness of the layer thickness above the décollement, T, as obtained from Eq. (3), shows large dispersion (within more than one order of magnitude).

Moreover, the T values are surprisingly large considering push-up sizes. We infer that the estimates presented in Table 1 are unreliable, probably because the simplifying assumptions made were not valid.

6. Limitations and pitfalls in simple evaluations of push-up shortening

Making the assumption that $W_0 = L$, as in Table 1, is in fact unacceptable (Fig. 7). Assuming that the present-day and pre-earthquake volumes are equal (so that $S = S^*$) is also unacceptable.

First, minor thrusts and second-order folds may affect push-ups (Fig. 7b). The measured value of L may thus be substantially smaller than the actual initial width, W_0. Such an internal shortening was illustrated by minor thrusts and tight folds for an oblique thrust of the 1999 earthquake in Taiwan (Angelier et al., 2003b). In the Icelandic push-ups, small thrusts or minor folds remain unnoticed, because they occur near the push-up base where grassy soil makes observation difficult. On the contrary, where open fissures affect the summit of the push-up (Fig. 7b), correction can be done based on observation of some outcrops.

The second major source of uncertainty results from the gravitational deformation of push-ups that begins during the earthquake and continues during the post-seismic period. The push-ups created during a major earthquake progressively collapsed (Bjarnason et al., 1993). This effect is
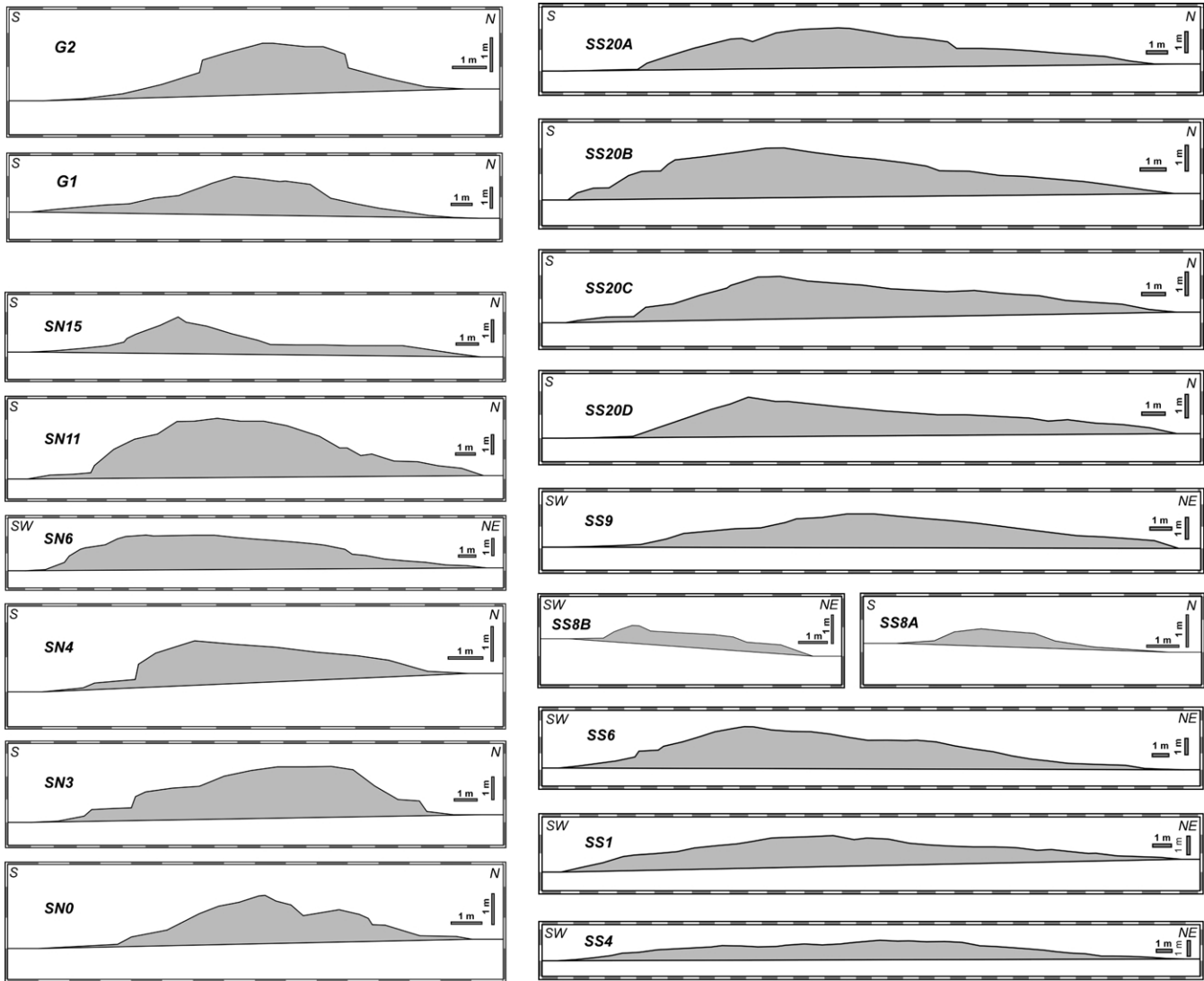
Fig. 8. Cross-sections of push-ups along the Gerdi (G), N-Selsund (SN) and S-Selsund (SS) segments of the Selsund rupture trace generated by the 1912 earthquake. Location in Fig. 4. Topographic profiles with the same reference numbers as in the map of Fig. 4 and Tables 1–4.

explained by the instantaneous mechanical dilatation that affects the mass of the push-up during the earthquake and creates open gaps (Fig. 7b). Push-up inflation during the earthquake is followed by compaction after the earthquake (Fig. 7c). Most of the gravitational process is achieved during the first weeks or months after the earthquake. Relict gaps between broken basalt slabs are still observable in hillocks, indicating that the sagging has not compensated the extra volume. These volume changes bias the determination of W_0 and S^*.

The co-seismic and post-seismic changes in push-up shape and volume are unknown. We can only compare the present-day configuration of the push-ups with the pre-earthquake configuration (that is, the flat upper surface of the lava fields, tuff layers and soils where the earthquake rupture developed). This approach requires determination of the relation between L and W_0, which cannot be done, or between S and S^*, which is the basis of our study.

The comparison between the pre-earthquake and present-day configurations is highlighted by consideration of average density of the whole push-up, which includes rock and open gaps (Fig. 9). The final volume of deformed rock is S_T, whereas the corresponding initial volume of intact rock is S_T^* (volume per unit length of push-up). Note that the virtual stage shown in Fig. 9b, lacking co-seismic dilatation and collapse, differs from the real situation of Fig. 7b. Note also that contrary to S and S^*, the volumes S_T and S_T^* include both the hillock and the underlying rocks involved in the push-up structure down to the inferred décollement level. The average ratio, λ_a, between the present-day and pre-earthquake densities, is the ratio between the pre-earthquake and present-day volumes:

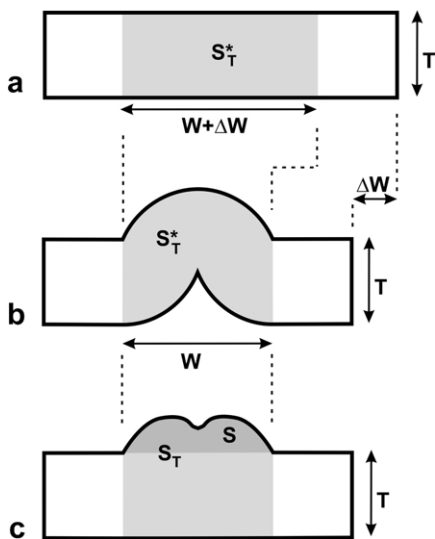$$\lambda_a = \frac{S_T^*}{S_T} \tag{5}$$

Fig. 9. Scheme used for the determination of the relationship between shortening, ΔW, and thickness of the deformed layer, T. S-values refer to volumes (in grey) per unit length of push-up, measured in transverse cross-sections. (a) Pre-earthquake stage. S_T^*, in grey: total volume. (b) Virtual stage after co-seismic deformation without volume change or collapse. The total volume, in grey, is also S_T^*. (c) Present-day stage after co-seismic and post-seismic deformation, volume changes and collapse: S_T, volume after co-seismic dilation and collapse during and after the earthquake (whole grey area); S, hillock volume (in dark grey).

Evaluation of the rock state could not be done inside and beneath the push-ups. It was obtained in few outcrops near push-up tops, where disruption is largest and gaps still exist 90 years after the 1912 earthquake because of the rigidity of the broken basalt slabs. We evaluated an average near-surface ratio, λ_s, of 0.9 ($\pm 5\%$). The uncertainty comes from the difficulty of comparing volumes of rock and gaps. The link between λ_s (near push-up top) and λ_a (whole push-up) will be considered in Section 7. In soils and tuffs where collapse and compaction nearly restored the initial rock density, an average λ_s value of 0.95 ($\pm 5\%$) can be evaluated. Based on the composition of all push-ups, the mean value is $\lambda_s = 0.90 \pm 0.05$.

Beneath the hillock, the volume per unit length of deformed rock equals the depth of the inferred décollement, T, multiplied by the push-up width, W. The total section of deformed rock, S_T, is obtained by adding this section, WT, to that of the hillock, S (Fig. 7). S_T is greater than S, and depends not only on the data S and W, but also on the unknown T.

Assuming $W_0 = L$, Eq. (2) provided unreliable push-up shortening values. In fact, L may be significantly smaller than W_0. This explains why small values of ΔW and D were obtained in Table 1, large values of T being subsequently given by Eq. (3). Similarly, the excess section of the hillock without volume change, S^*, is not the observed section, S. The relationships between L and W_0, and between S and S^*, thus deserve careful examination.

7. Relationship between push-up shortening and layer thickness

Fig. 9 summarises the evolution of a push-up. During the pre-earthquake stage (Fig. 9a), the future push-up domain corresponds to a width $W + \Delta W$ and a layer thickness T, with ΔW and T being the unknowns. The volume per unit length, S_T^*, is given by:

$$S_T^* = T(W + \Delta W) \tag{6}$$

A virtual section shows the push-up structure assuming a constant rock volume and no collapse (Fig. 9b). In contrast, co-seismic dilatation and initial collapse affect the actual cross-section of Fig. 7b. The present-day configuration is summarised in Fig. 9c. Because of volume changes during and after the earthquake, it involves a volume S_T larger than the deformed rock volume S_T^*. From Eq. (5) and definition of S_T (Fig. 9a), one obtains:

$$S_T^* = \lambda_a(S + WT) \tag{7}$$

Combining Eqs. (6) and (7), one obtains a single relation between the two unknowns of the problem, ΔW and T, with parameters that depend on the data:

$$\Delta W = \lambda_a S \frac{1}{T} - (1 - \lambda_a)W \tag{8}$$

The determination of the average density ratio of the whole push-up structure, λ_a, is crucial. The variable density ratio at each point of the structure, λ, depends on the dilatation and collapse, which are proportional to the amount of deformation (zero around the push-up and maximum at push-up crest). At the surface, λ equals one in the flat domain surrounding the push-up, and reaches a minimum value, λ_s, at the push-up top. The variation of λ in push-up flanks was considered proportional to relative elevation in the first approximation. With depth, λ increases, reaching one at the décollement level; a linear variation was adopted as a reasonable approximation of the progressive diminution of void volumes. The value of λ was calculated at each point between the surface and the décollement, giving λ_a as follows:

$$\lambda_a = \frac{\sum_{k=1}^{k=K} w_k(T + q_k)\left[\frac{1}{2}(\lambda_s - 1)\frac{q_k}{q_{max}} + 1\right]}{S_T} \tag{9}$$

where the index k is the reference number of the profile segment, from one to K, w_k is the segment width and q_k refers to segment height above the oblique push-up base shown in the profiles of Fig. 8 (q_{max} corresponds to push-up top). In each profile, the λ_a value given by Eq. (9) did not change significantly as a function of T, so that a single value of λ_a could be adopted for each push-up (Table 2). Despite high ratios λ_a (0.97–0.98), this volumetric correction is significant because the deformed section is larger than the hillock section.
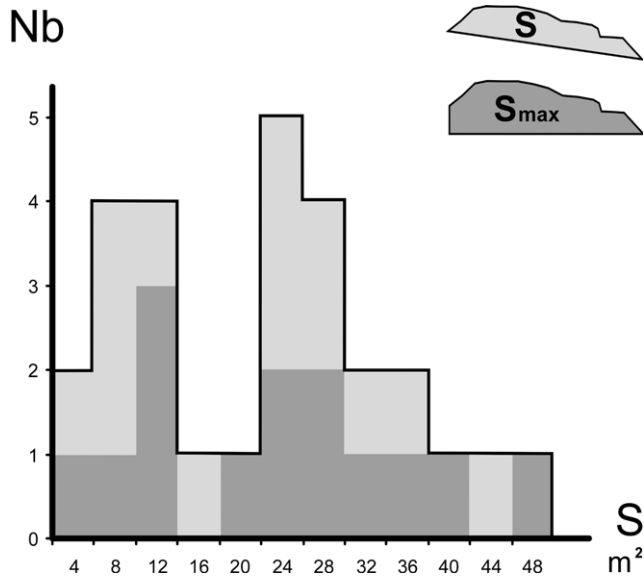
Fig. 10. Bimodal distribution of present-day volumes of push-up hillocks: *Nb*, number of push-ups; *S*, volume per unit length, measured in two ways (*S*, oblique base; S_{max}, horizontal base, see schematic illustration in upper-right corner), and listed in Table 1.

The strike–slip displacement, *D*, is obtained by combining Eqs. (1) and (8):

$$D = \frac{a}{T} - b \tag{10}$$

with

$$a = \frac{\lambda_a S}{\cos\theta}$$

and

$$b = \frac{(1 - \lambda_a)W}{\cos\theta}.$$

Table 2 gives, for each profile, the coefficients *a* and *b* of the linear relationship (10) between *D* and T^{-1}, as well as their standard deviations. Table 2 also indicates, for each push-up, the largest acceptable layer thickness, T_{max}. The values range between 11 and 55 m (33 m on average). They are smaller and show less dispersion than the values obtained without correction (Table 1), which ranged between 11 and 209 m (57 m on average).

8. Comparisons between push-ups

A numerical inversion was performed, with *D* and *T* as common variables. The four bracketed push-ups of Table 2 were omitted (see Section 5). Ten equations of type (10) were thus available. As *T* increases, the maximum value that still accounts for all the data is *T* = 27 m (giving a minimum of 0.28 m for *D*). The bimodal distribution of push-up volumes per unit length, with a separation near 16–20 m²
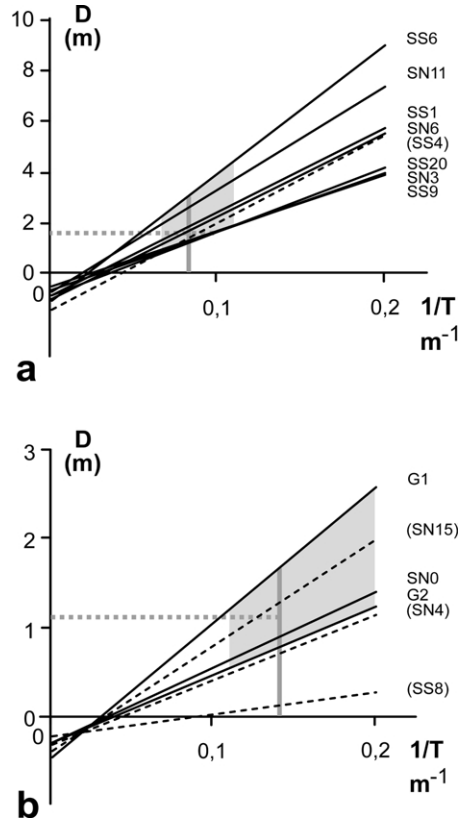

Fig. 11. Linear relationships between the strike–slip displacement, *D*, and the inverse of the deformed layer thickness, T^{-1}, according to Eq. (10) and parameters of Table 2. (a) and (b) Large and small push-ups, respectively (see Fig. 10). Push-up names as in Table 2. Push-ups with bracketed names correspond to dashed lines, indicating data that do not reflect displacement on main fault segment but yield minimum values. In grey: domains with acceptable thickness, *T*, of deformed layer. Grey dotted line indicates average displacement.

Table 2
Parameters λ_a, *a* and *b* calculated according to Eqs. (9) and (10), with $\lambda_s = 0.9$. Same push-ups and values of *W* and *S* as in Table 1 and Fig. 8. Bracketed values refer to push-ups that do not account for main fault displacement (see Sections 5 and 8 of text). Values averaged for push-ups with two or more profiles: Δa and Δb, standard deviations of *a* and *b*; T_{max}, largest possible value of *T*, calculated from Eq. (10) with *D* = 0

Ref.	λ_a	*a* (m²)	Δa (m²)	*b* (m)	Δb (m)	T_{max} (m)
G2	0.98	7.61	0.48	0.28	0.43	27
G1	0.98	15.26	0.83	0.46	0.63	33
(SN15)	(0.98)	(11.94)	(0.78)	(0.39)	(0.65)	(31)
SN11	0.97	40.37	2.45	0.73	0.91	55
SN6	0.97	32.91	2.06	0.87	1.04	38
(SN4)	(0.97)	(7.32)	(0.45)	(0.31)	(0.42)	(24)
SN3	0.97	21.95	1.17	0.53	0.66	42
SN0	0.98	8.51	0.60	0.29	0.57	29
SS20	0.98	23.33	1.34	0.67	0.87	35
SS9	0.97	25.32	1.58	0.86	1.00	30
(SS8)	(0.98)	(2.46)	(0.21)	(0.22)	(0.32)	(11)
SS6	0.97	50.50	2.95	1.06	1.34	48
SS1	0.97	32.72	2.10	1.04	1.27	32
(SS4)	(0.97)	(34.40)	(2.50)	(1.44)	(1.70)	(24)

Table 3
Results of determinations of the strike–slip displacement, D, according to Eqs. (9) and (10), with $\lambda_s = 0.9$ and $T = 7 \pm 2$ m (small push-ups) or $T = 12 \pm 3$ m (large push-ups). Same push-up profiles and values of W and S as in Table 1 and Fig. 8. Total volumes of deformed layer per unit length as S_T (present-day) and S_T^* (before earthquake) given for the same ranges of T. Values of the displacement, D, with standard deviations

Ref.	T (m)	S_T (m^2)	S_T^* (m^2)	D (m)
G2	7 ± 2	95 ± 25	93 ± 25	0.81 ± 0.49
G1	7 ± 2	164 ± 42	160 ± 41	1.72 ± 0.81
SN15	7 ± 2	152 ± 41	148 ± 40	1.32 ± 0.72
SN11	12 ± 3	311 ± 69	303 ± 67	2.64 ± 1.10
SN6	12 ± 3	351 ± 80	341 ± 77	1.88 ± 1.20
SN4	7 ± 2	93 ± 24	90 ± 24	0.74 ± 0.48
SN3	12 ± 3	258 ± 58	251 ± 58	1.30 ± 0.76
SN0	7 ± 2	107 ± 28	105 ± 28	0.92 ± 0.65
SS20A	12 ± 3	375 ± 87	366 ± 85	1.46 ± 1.07
SS20B	12 ± 3	306 ± 80	297 ± 68	1.36 ± 0.97
SS20C	12 ± 3	332 ± 77	323 ± 75	1.23 ± 0.95
SS20D	12 ± 3	333 ± 78	325 ± 75	1.04 ± 0.93
SS9	12 ± 3	360 ± 84	351 ± 82	1.25 ± 1.12
SS8A	7 ± 2	61 ± 17	59 ± 16	0.09 ± 0.29
SS8B	7 ± 2	62 ± 16	60 ± 16	0.18 ± 0.39
SS6	12 ± 3	502 ± 114	489 ± 111	3.15 ± 1.57
SS1	12 ± 3	427 ± 101	415 ± 97	1.69 ± 1.43
SS4	12 ± 3	507 ± 119	492 ± 116	1.43 ± 1.86

(Fig. 10), suggests that large push-ups be rooted at deeper levels than small ones. A numerical inversion done with the seven large push-ups gave $T = 29$ m (high bound) and $D = 0.30$ m (low bound). Introducing the latter D value in Eq. (10) yielded a maximum T value of 13–14 m for the three small push-ups. Considering these bounds, the bimodal size distribution and other constraints (including individual push-up sizes and shapes), the inferred thickness of the layer affected by push-ups averages 12 m for large push-ups (Fig. 11a) and 7 m for small ones (Fig. 11b). Uncertainties reach 23 m. Because there is no significant difference in structure between these push-ups, we infer that these two T values, 7 and 12 m, reflect different numbers of lava flows involved in the deformation.

Based on the relationships (9) and (10), all strike–slip displacements were calculated again (Table 3). The resulting values are larger than in Table 1 and their dispersion is smaller. For the 10 push-ups that presumably recorded motion of the main fault, the results indicate a strike–slip displacement, D, of 1.66 ± 1 m on average (Fig. 12a). This value is larger than the value of 1.25 m obtained by Bjarnason et al. (1993) 'from the two largest push-ups'.

9. The push-up model

A geometrical model of the push-up structure was built as a virtual section according to the scheme of Fig. 9b. The volume change and collapse effects during and after the earthquake are ignored. Such a model needs to be simple, to avoid uncontrolled variables that depend on the unknown history of volume changes and collapse (Fig. 7). The only reliable information that constrains the model comes from the present-day cross-sections.

Two versions involve fold segments as circular arcs (Fig. 13a) or straight fold flanks (Fig. 13b), both with concentric folding mode. These sub-models reflect end-members of the deformation patterns observed: gently folded tuff and soil layers, or rigid broken basalt slabs. Four elements differ in radius, r_i. As an approximation, the horizontal width, w_i, of each element has not been affected by volume changes and collapse, and thus can be measured in the present-day profile. Fold angles, α and β, characterises the two elements of each push-up flank. The radii of these two elements depend on the unknown height of the virtual push-up structure, $h_1 + h_2$ or $h_3 + h_4$. These heights changed, but their difference, E, remained constant and is measured in the present-day profile (Table 1). To constrain the virtual push-up heights, we determine the theoretical volume per unit length, S_T^* (Table 3; in grey in Fig. 13):

$$S_T^* = T[F(\alpha)(w_1 + w_2) + F(\beta)(w_3 + w_4)] \qquad (11)$$

where F is a function that depends on the folding sub-mode, F_a (Fig. 13a) or F_b (Fig. 13b). With ω as a dummy variable in radians, one writes:

$$F_a(\omega) = \frac{\omega}{\sin\omega}, \qquad F_b(\omega) = \frac{2\mathrm{tg}\frac{\omega}{2}}{\sin\omega} \qquad (12)$$

The present-day difference in elevation between profile tips, E, is:

$$E = \frac{w_1 + w_2}{\mathrm{tg}\frac{\alpha}{2}} - \frac{w_3 + w_4}{\mathrm{tg}\frac{\beta}{2}} \qquad (13)$$

The geometrical model is constrained solving the system of Eqs. (11) and (13) to get α and β, and then calculating the radii, r_i, and the vertical distances, h_i, as a function of these angles and distances w_i (Fig. 13). The shortening, ΔW, is given by Eq. (2), W_0 being extracted from the model. Eq. (1) gives the fault displacement, D, so that:

$$D = \frac{F(\alpha)(r_1 + r_2) + F(\beta)(r_3 + r_4) - (w_1 + w_2 + w_3 + w_4)}{\cos\theta} \qquad (14)$$

The values of D given by Eq. (14) are the same as in Table 3. The peak amount of collapse, C (Table 4) is the difference between the push-up height calculated from the model and the present height (Table 1). The largest uncertainty comes from T (± 2–3 m).

Depending on the folding sub-mode, two subsets of values were obtained for α, β and C. They are shown in
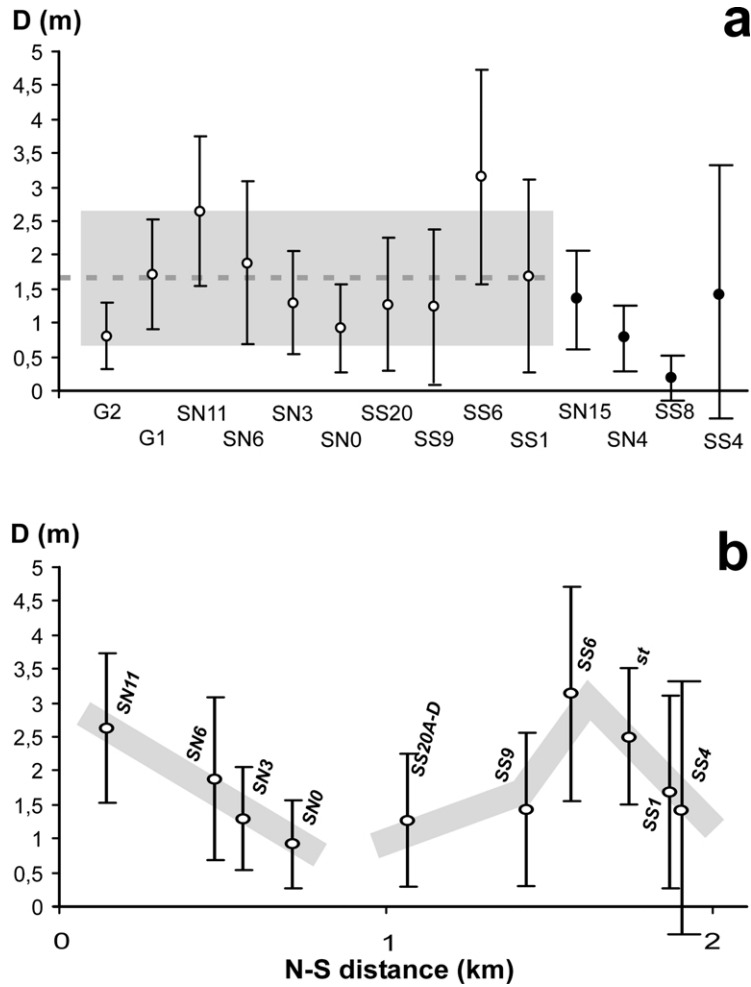
Fig. 12. Summary of our determinations of the strike–slip displacement, D, along the Selsund Fault, based on structural analysis of push-ups (Table 3). Open dots refer to push-ups that accommodate the main fault motion during the 1912 earthquake; solid dots refer to other push-ups (see Section 10 of text). (a) Raw results for all push-ups (from north to south, without horizontal scale). In grey: average displacement (dashed line) and standard deviation. (b) Along-strike variations in shortening for push-ups accommodating main fault motion (N-Selsund and S-Selsund segments). Note incorporation of push-up SS4 (details in text).

Table 4 with indexes a and b, respectively, referring to the models a and b of Fig. 13 and the functions F_a and F_b of Eq. (12). The values of C_a range from 0.1 to 7.7 m (2.6 m on average), whereas the values of C_b range from 0 to 5.7 m (1.8 m on average). In addition to the post-seismic sagging, the C values include the co-seismic collapse (Fig. 7b). Thus, the push-up height never reached the maximum value predicted by the model, because the virtual push-up structure (Figs. 9b and 13) was never achieved.
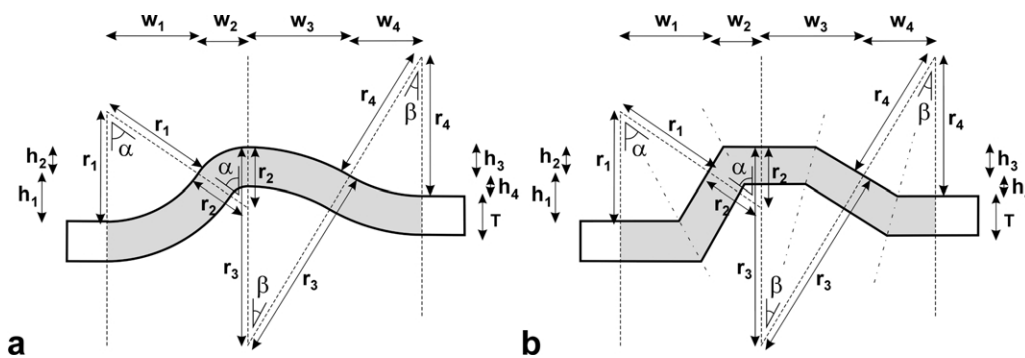

Fig. 13. The push-up model. Concentric folding, with elements as circular arcs (a) or straight segments (b). Virtual section according to the principle of Fig. 9b. Push-up domain in grey: T, constant layer thickness; r_i, w_i, and h_i, radii, horizontal width and height of element i ($i = 1,4$), respectively; α and β, fold angles of the left and right push-up flanks, respectively.

Table 4
Main results of determinations of push-up structure, based on the concentric folding model of asymmetrical push-up. Angles α and β defined in Fig. 13: C, largest possible collapse at push-up top; Indexes a and b refer to the two sub-models of Fig. 13, with flanks as arcs of circles (a) or straight lines (b). Standard deviations given for $T = 7 \pm 2$ m (small push-ups) or $T = 12 \pm 3$ m (large push-ups). Other parameters as in Table 3

Ref.	α_a (°)	β_a (°)	C_a (m)	α_b (°)	β_b (°)	C_b (m)
G2	37 ± 7	33 ± 6	0.55 ± 0.45	30 ± 6	27 ± 5	0.12 ± 0.30
G1	37 ± 7	41 ± 7	2.20 ± 0.80	30 ± 6	33 ± 6	1.39 ± 0.63
SN15	18 ± 4	38 ± 7	3.00 ± 0.94	15 ± 3	31 ± 5	2.08 ± 0.74
SN11	35 ± 5	47 ± 7	2.71 ± 0.98	28 ± 4	38 ± 6	1.57 ± 0.76
SN6	16 ± 3	40 ± 7	4.85 ± 1.32	13 ± 2	32 ± 6	3.52 ± 1.06
SN4	23 ± 5	39 ± 7	1.26 ± 0.58	18 ± 4	32 ± 6	0.73 ± 0.47
SN3	40 ± 7	23 ± 4	2.24 ± 0.85	33 ± 5	18 ± 3	1.34 ± 0.67
SN0	36 ± 6	35 ± 6	0.58 ± 0.45	29 ± 5	28 ± 5	0.14 ± 0.29
SS20A	27 ± 5	33 ± 6	2.69 ± 0.92	22 ± 4	27 ± 5	1.79 ± 0.74
SS20B	20 ± 4	38 ± 7	3.29 ± 1.03	16 ± 3	31 ± 5	2.27 ± 0.82
SS20C	18 ± 4	34 ± 7	3.27 ± 1.06	15 ± 3	28 ± 6	2.27 ± 0.84
SS20D	13 ± 4	32 ± 6	3.52 ± 1.08	10 ± 2	26 ± 5	2.53 ± 0.86
SS9	26 ± 5	28 ± 6	2.14 ± 0.81	21 ± 4	23 ± 5	1.43 ± 0.64
SS8A	8 ± 4	16 ± 9	0.07 ± 0.33	7 ± 3	14 ± 7	0.00 ± 0.26
SS8B	9 ± 4	23 ± 8	0.16 ± 0.32	7 ± 3	18 ± 6	0.00 ± 0.29
SS6	19 ± 3	42 ± 8	7.69 ± 1.56	15 ± 3	35 ± 5	5.70 ± 1.42
SS1	25 ± 5	32 ± 7	3.48 ± 1.15	20 ± 4	27 ± 5	2.45 ± 0.91
SS4	25 ± 6	22 ± 5	3.31 ± 1.19	20 ± 5	18 ± 4	2.44 ± 0.95

10. Discussion and conclusion

Our results along the rupture trace of the 1912 Selsund earthquake (Fig. 12) highlight the potential of structural analyses of push-ups to reveal the amount of displacement along earthquake strike–slip faults. Neglecting the volume changes and collapse effects results in unreliable determination of strike–slip displacement (Table 1), with unacceptable dispersion and underestimated displacement, D (e.g. 0.71 m instead of 1.66 m). This comparison shows that one cannot ignore the internal structure of the push-up structures, nor neglect the effects of volume changes and collapse that affected the push-ups during and after the earthquake.

To this respect, a major element is the thickness of the layer involved in the push-up structure (Fig. 11). Two contrasting values, $T = 7 \pm 2$ and 12 ± 3 m, were estimated along the Selsund Fault (Table 3), consistent with the bimodal distribution of push-up sizes (Fig. 10). Considering the succession of the Holocene lava flows intersected by the fault, these values reflect the thicknesses of the uppermost volcanic units. Despite the consistency of our final determinations of D (Table 3 and Fig. 12a), a large uncertainty still exists because the calculation of T lacks accuracy in the absence of direct observation.

A deformed section thicker than 12 m may locally exist, as suggested by the large extent and limited height of push-up SS4. Interestingly, the push-up SN15, on a minor left-lateral conjugate fault (Fig. 9a), allowed the determination of a strike–slip displacement that nearly equals that of the right-lateral main fault (Fig. 12). Not surprisingly, the push-
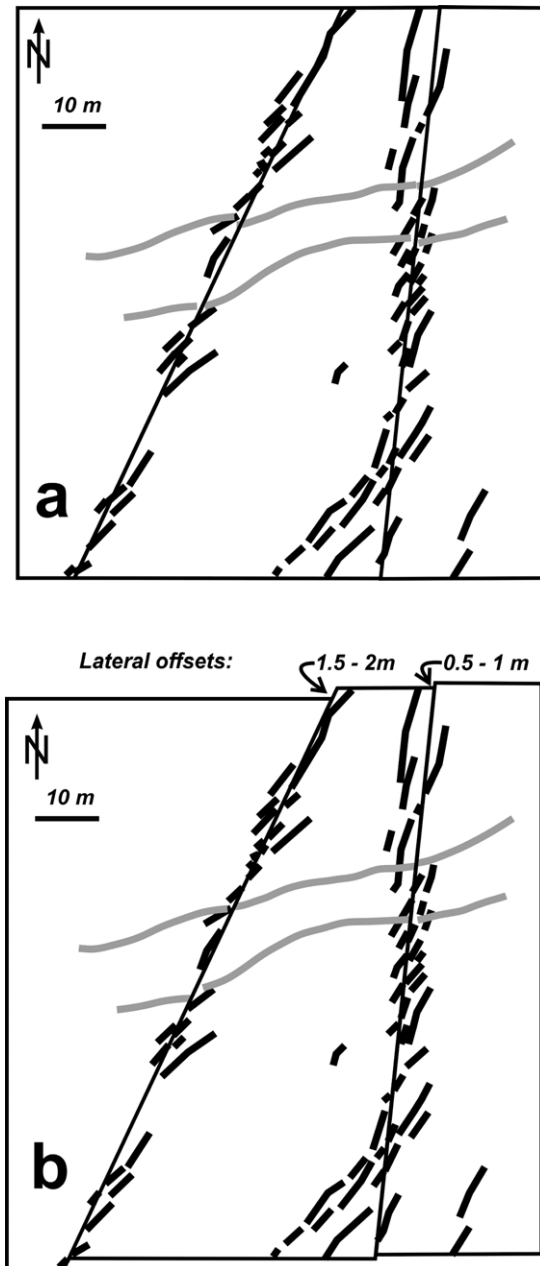

Fig. 14. (a) Map of sheep tracks (grey lines) offset by the 1912 rupture trace, S-Selsund fault segment (location in Fig. 4). Fissures as thick black lines. (b) Restoration of track continuity obtained with a total left-lateral displacement of 2–2.5 m.

ups SN4 and SS8, located on a subsidiary right-lateral fault, underwent less contraction than the main strike–slip motion would have implied. These different behaviours show that mapping of earthquake rupture traces is essential to determine whether or not the entire strike–slip displacement was absorbed by each push-up.

The strike–slip displacement, D, is not uniform but varies along strike. The calculated values increase from south to north along the N-Selsund segment, suggesting a northern extension of this segment; they also increase towards the central portion of the S-Selsund segment

(Fig. 12b). We infer that the peak slip, D_{max}, of the 1912 earthquake is probably best represented by combining the results from push-ups SN11–SN6 ($D_{max} = 2.26 \pm 1.15$ m) for the N-Selsund segment, and push-ups SS6–SS1 ($D_{max} = 2.42 \pm 1.50$ m) for the S-Selsund segment.

Our results can be compared with the earlier determinations by Bjarnason et al. (1993). Along the N-Selsund fault segment, these authors determined a maximum slip of 1.25 m 'from the two largest push-ups'. We obtained a significantly larger value, 1.69 ± 0.93 m, from four push-ups that accommodated motion along this segment (Table 3). Our general result also indicates a larger value, 1.66 ± 1.00 m, from 10 push-ups of variable size.

Bjarnason et al. (1993) measured a displacement of 3 m across the S-Selsund segment, based on the offset of deeply worn sheep tracks. The tracks were continuously used, so that the offset is still observable 90 years after the earthquake. We mapped the rupture trace and sheep tracks with the differential GPS (Fig. 14a). The restoration of continuous tracks requires a displacement of 2.5 ± 0.5 m (Fig. 14b). This site is located between push-ups SS6 and SS1 where push-ups indicated the largest offset, $D_{max} = 2.42 \pm 1.50$ m (Fig. 12b). Thus, the independent observation of sheep tracks brings the only available validation of our results.

Summing up, the right-lateral displacement of the 1912 Selsund earthquake averaged 1.7 m from the 10 push-ups analysed. Uncertainties are, however, as large as about 1 m. The peak slip reached about 2.4 m. Wells and Coppersmith (1994) derived the following relationship between the moment magnitude, M, and the peak displacement in metres, D_{max}:

$$M = 6.81 + 0.78\log_{10}D_{max} \tag{15}$$

Based on the peak slips that we determined for the two Selsund segments, 2.4 ± 1 m on average, we obtain a magnitude 7.1 ± 0.15, compatible with the instrumentally recorded magnitude of the Selsund earthquake, approximately 7 as given by Karnik (1969). A relationship between the maximum displacement and the surface-wave magnitude (Ambraseys and Jackson, 1998) yielded a similar magnitude range (6.9–7.2). One may question the validity of such general laws in the particular context of a thin oceanic crust. However, the data of the June 2000 earthquakes in the SISZ well fitted these empirical relationships, suggesting that they are valid in South Iceland (Bergerat and Angelier, 2001, 2003; Bergerat et al., 2003). A critical aspect in seismic hazard studies deals with the evaluation of the largest earthquake magnitudes that may occur in an active tectonic zone. One century of instrumental records cannot tightly constrain the largest expectable magnitudes. The Leirubakki Fault (Fig. 2b) resulted from a post-glacial earthquake, presumably one of the largest earthquakes having left surface traces in the SISZ. The determination of strike–slip displacement along this fault suggested a moment magnitude of about 7.1 (Bergerat et al., 2003). In the absence of historical or instrumental information this determination could not be checked. While analysing the push-ups of the Leirubakki Fault, the volume changes and collapse effects were neglected. Considering the output of the new method along the Selsund Fault, a strike–slip displacement larger than the estimated one may be expected for the Leirubakki earthquake, which would increase the largest expectable earthquake magnitudes in South Iceland.

Acknowledgements

References

Ambraseys, N.N., Jackson, J.A., 1998. Faulting associated with historical and recent earthquakes in the eastern Mediterranean region. Geophysical Journal International 133, 390–406.

Angelier, J., Bergerat, F., 2002. Behaviour of a rupture of the June 21st, 2000, earthquake in South Iceland as revealed in an asphalted car park. Journal of Structural Geology 24, 1925–1936.

Angelier, J., Lee, J.-C., Chu, H.-T., Hu, J.-C., 2003a. Reconstruction of fault slip of the September 21st, 1999, Taiwan earthquake in the asphalted surface of a car park, and co-seismic slip partitioning. Journal of Structural Geology 25, 345–350.

Angelier, J., Lee, J.-C., Hu, J.-C., Chu, H.-T., 2003b. Three-dimensional deformation along the rupture trace of the September 21st, 1999, Taiwan earthquake: a case study in the Kuangfu school. Journal of Structural Geology 25, 351–370.

Bellou, M., 2002. Sismotectonique de la Zone Sismique Sud-Islandaise: géométrie et mécanisme des failles majeures. Unpubl. Master Thesis (DEA) Memoir, July 4th, 2002, Université Pierre-et-Marie Curie, Paris, 42pp.

Bergerat, F., Angelier, J., 1999. Géométrie des failles et régimes de contraintes à différents stades de développement des zones transformantes océaniques: exemples de la zone sismique sud-Islandaise et de la zone de fracture de Tjörnes (Islande). Comptes Rendus de l'Académie des Sciences, Paris 329, 653–659.

Bergerat, F., Angelier, J., 2000. The South Iceland Seismic Zone: tectonic and seismotectonic analyses revealing the evolution from rifting to transform motion. Journal of Geodynamics 29, 211–231.

Bergerat, F., Angelier, J., 2001. Mécanismes des failles des séismes des 17 et 21 Juin 2000 dans la Zone Sismique Sud-Islandaise d'après les traces de surface des failles d'Árnes et de l'Hestfjall. Comptes Rendus de l'Académie des Sciences, Paris 333, 35–44.

Bergerat, F., Angelier, J., 2003. Mechanical behaviour of the Árnes and Hestfjall Faults of the June 2000 earthquakes in Southern Iceland: inferences from surface traces and tectonic model. Journal of Structural Geology 25, 1507–1523.

Bergerat, F., Gudmundsson, A., Angelier, J., Rögnvaldsson, S.Th., 1998. Seismotectonics of the central part of the South Iceland Seismic Zone. Tectonophysics 298, 319–335.

Bergerat, F., Angelier, J., Gudmundsson, A., Torfason, H., 2003. Push-ups, fracture patterns and palaeoseismology of the Leirubakki Fault, South Iceland. Journal of Structural Geology 25, 591–609.

Bjarnason, I.Th., Cowie, P., Anders, M.H., Seeber, L., Scholz, C.H., 1993. The 1912 Iceland earthquake rupture: growth and development of a nascent transform system. Bulletin of the Seismological Society of America 83, 416–435.

Björnsson, S., 1975. Earthquakes in Iceland. Náttúrufraedingurinn 45, 110–133. (in Icelandic).

DeMets, C., Gordon, R.G., Argus, F., Stein, S., 1990. Current plate motions. Geophysical Journal International 101, 425–478.

DeMets, C., Gordon, R.G., Argus, F., Stein, S., 1994. Effect of recent revisions to the geomagnetic reversal time scale on estimates of current plate motions. Geophysical Research Letters 21, 2191–2194.

Einarsson, P., 1991. Earthquakes and present-day tectonism in Iceland. Tectonophysics 189, 261–279.

Einarsson, P., Björnsson, S., 1979. Earthquakes in Iceland. Jökull 29, 37–43.

Einarsson, P., Eiriksson, J., 1982. Jardskjalftasprungur á Landi og Rangarvöllum. In: Eldur er i nordri, Sögufélag, Reykjavik, pp. 295–310.

Einarsson, P., Eiriksson, J., 1982b. Earthquake fractures in the districts Land and Rangárvellir in the south Iceland seismic zone. Jökull 32, 113–120.

Einarsson, P., Björnsson, S., Foulger, G., Stefansson, R., Skaftadottir, Th., 1981. Seismicity pattern in the South Iceland Seismic Zone. In: Simpson, D.W., Richards, P.G. (Eds.), Earthquake Prediction: An International Review, AGU Maurice Ewing Series 4, Washington DC, pp. 141–151.

Gudmundsson, A., 1995. Ocean-ridge discontinuities in Iceland. Journal of the Geological Society 152, 1011–1015.

Gudmundsson, A., Brynjolfsson, S., 1993. Overlapping rift-zone segments and the evolution of the South Iceland Seismic Zone. Geophysical Research Letters 20, 1903–1906.

Jóhannesson, H., Jakobsson, S. P., Saedmundsson, K., 1990. Geological map of Iceland, sheet 6, south Iceland. Icelandic Museum of Natural History and Iceland Geodetic Survey, Reykjavik, scale 1:250,000.

Karnik, V., 1969. Seismicity of the European Area, Part I, Reidel, Dordrecht, Holland.

Riedel, W., 1929. Zur Mechanik geologischer Brucherscheinungen. Zentralblatt für Mineralogie, Geologie und Paläontologie 1929B, 354–368.

Saemundsson, K., 1979. Outline of the geology of Iceland. Jökull 29, 7–28.

Stefansson, R., 1979. Catastrophic earthquakes in Iceland. Tectonophysics 53, 273–278.

Stefansson, R., Bödvarsson, R., Slunga, R., Einarsson, P., Jakobsdottir, S.S., Bungum, H., Gregersen, S., Havskov, J., Hjelme, J., Korhonen, H., 1993. Earthquake prediction research in the South Iceland Seismic Zone and the SIL project. Bulletin of the Seismological Society of America 83, 696–716.

Tchalenko, J.S., Ambraseys, N.N., 1970. Structural analysis of the Dasht-e-Bayaz (Iran) earthquake fractures. Geological Society of America Bulletin 81, 41–60.

Tryggvason, K., Husebye, E., Stefansson, R., 1983. Seismic image of the hypothesized Icelandic hot spot. Tectonophysics 100, 97–118.

Wells, D.L., Coppersmith, K.J., 1994. New empirical relationships among magnitude, rupture length, rupture width, rupture area, and surface displacement. Bulletin of the Seismological Society of America 84, 974–1002.